

Localized Structures in a Diffusive Run-and-Tumble Model of *Myxococcus xanthus*

By
Patrick Flynn

A THESIS

submitted to

Oregon State University

University Honors College

in partial fulfillment of
the requirements for the
degree of

Honors Baccalaureate of Science in Mathematics and Physics
(Honors Scholar)

Presented May 16, 2018
Commencement June 2018

AN ABSTRACT OF THE THESIS OF

Patrick Flynn for the degree of Honors Baccalaureate of Science in Mathematics
and Physics presented on May 16, 2018. Title:

Localized Structures in a Diffusive Run-and-Tumble Model of *Myxococcus xanthus*

Abstract approved:

Arnd Scheel

The bacteria *Myxococcus xanthus* clusters into fruiting bodies in the absence of food. The movement of *M. xanthus* has three aspects: self-propulsion (run), change of direction due to collision (tumble), and Brownian fluctuations in movement. We propose a minimalist PDE model for the concentrations of left and right moving agents in one-dimension that incorporates these three phenomena as advection, diffusion and reaction respectively. We proceed to analyze stationary solutions to this equation, utilizing geometry and dynamical systems theory to show existence of families of concentration profiles representing localized peaks or troughs in an otherwise uniform concentration. We verify and extend these existence results by computing cluster and gap type solutions with numerical continuation methods. We also demonstrate temporal stability of the clusters and gaps with numerical experiments. Phenomenologically, we find that these profiles form due to a combination of the left moving population blocking the forward movement of the right moving population and vice-versa, and dampening due to diffusion.

Key Words: mathematical biology, differential equations, dynamical systems

Corresponding e-mail address: flynpa@oregonstate.edu

©Copyright by Patrick Flynn
May 18, 2018
All Rights Reserved

Localized Structures in a Diffusive Run-and-Tumble Model of *Myxococcus xanthus*

By
Patrick Flynn

A THESIS

submitted to

Oregon State University

University Honors College

in partial fulfillment of
the requirements for the
degree of

Honors Baccalaureate of Science in Mathematics and Physics
(Honors Scholar)

Presented May 16, 2018
Commencement June 2018

Honors Baccalaureate of Science in Mathematics and Physics project of Patrick Flynn presented on May 16, 2018

APPROVED:

Arnd Scheel, Mentor, representing Mathematics (University of Minnesota)

Radu Dascaluc, Committee Member, representing Mathematics

Bo Sun, Committee Member, representing Physics

Toni Doolen, Dean, Oregon State University Honors College

I understand that my project will become part of the permanent collection of Oregon State University Honors College. My signature below authorizes release of my project to any reader upon request.

Patrick Flynn, Author

Contents

1	Introduction	2
2	Mathematical analysis	6
2.1	Observations for general tumbling rates	7
2.2	Head-on sensing	9
3	Numerical Methods	14
3.1	Numerical continuation	15
3.2	Homoclinic continuation	15
3.3	Heteroclinic continuation	17
3.4	Linear stability eigenvalue problem	18
3.5	Direct simulation	18
4	Numerical results & discussion	18
4.1	Homoclinic continuation	19
4.2	Heteroclinic continuation in the limit $\gamma \rightarrow 0$	21
4.3	Linear stability of homoclinic and heteroclinic solutions	22
4.4	Direct simulation of perturbed stationary profiles	24
4.5	Discussion	29
5	Conclusion	29
6	Appendix	30

List of Figures

1	Myxococcus and E. coli	2
2	Cluster continuation example	5
3	Trajectories in phase space	9
4	Unbounded Solutions	14
5	Families of homoclinics	20
6	Extrema of clusters and gaps v. background state	21
7	Heteroclinic profiles	22
8	Homoclinic spectra	23
9	Heteroclinic spectra and background concentration	24
10	Cluster instability	25
11	Gap instability	26
12	Instability of heteroclinic	27
13	Stability of cluster	28
14	Stability of front	28

1 Introduction



Figure 1: *Myxococcus xanthus* feeding on an *E. coli* colony and forming fruiting bodies (black spots) and ripples [1], with the earlier snapshot in the left. The large circular region contains stationary *E. coli*. To the left we have the region where the Myxobacteria began.

Understanding collective behavior of cells imposes one of the greatest challenges in biology, and an opportunity to apply physical and mathematical tools to describe complex biological systems. In this paper, we are interested in the macroscopic clusters formed by the common soil bacteria *Myxococcus xanthus*, referred to as myxobacteria. A myxobacteria colony forms two macroscopic stationary patterns: periodic ripples as the colony grows outward, and then central fruiting bodies (or clusters) once the colony has reached maximal extent; see figure 1 for snapshots from a video of myxobacteria preying on *E. coli* within a petri dish [1]. Unlike the equations of kinetic theory and fluid mechanics, there are no universally agreed upon first principles for models of the interactions and collective behavior of cell systems such as the myxobacteria. Nevertheless, we propose the formation of clusters can be explained by simple diffusion and run-and-tumble dynamics, only. The former is well-known to capture brownian movement of particles. The latter refers to systems exhibiting advection or transport (run) and change of the direction of transport (tumble). The model we consider in this paper originates from [2, 3], where such a model was used to describe the rippling behavior. With this minimalist mathematical model, we demonstrate the existence and stability of localized clusters (along with profiles representing local gaps in concentrations or interfaces between different concentrations) by employing a combination of analysis and numerical experiments.

Before embarking on a technical mathematical discussion, it is worthwhile to understand the motivation of modeling cell behavior, and the challenges that arise. Beyond just the myxobacteria, the ability for large populations of biological agents to act collectively carries fundamental scientific importance with regards to the origins of multicellular life or the social behavior of communities of organisms. Simultaneously,

we can approach the problem of modeling cells by using well established mathematical and physical tools, namely cellular automata, differential equations, kinetic theory and fluid mechanics. For instance, the ability of the slime mold *Dictyostelium discoideum* to form tissue-like structures out of individual cells via chemical signaling has been studied using a deformable ellipsoid model [4]. Another slime mold, *Physarum polycephalum* has a remarkable ability to find optimal paths and navigate mazes (this has been modeled in [5]). In fact, this ability of *P. polycephalum* has found application in discovering a Tokyo rail network superior to the one existing today [5]. The strange radial spiral patterns found in biofilms of the intestinal pathogen *Proteus mirabilis* was found to be driven by chemical signaling and cell motility via an experimentally verified model [6].

As with these examples, the ability for myxobacteria to form ripples and fruiting bodies is not just important for purely aesthetic reasons. Rather, these structures are an aspect of the life cycle of a myxobacteria colony: ripples form during periods of active growth and predatory consumption, while fruiting bodies appear in the absence of a food source [7]. Gene knockout experiments suggest that the biological mechanism behind these patterns is a combination of cell motility and the *C-signal* [8]. Each myxobacterium carries a surface protein called the *C-factor*—the C-signal causes reversal in the direction of travel when one bacterium makes direct contact with this protein. We call such collisions *tumbling events*.

These two mechanisms, self-propelled movement and collision, are well understood in the context of physics and mathematical modeling. The model we base our study on, originally proposed in [2], took the approach of considering the concentration of left moving agents u and right moving agents v throughout space and time. To simplify our model, we assume that a cell moves constantly at unit speed. Then, we can use the well-known transport equations

$$\frac{\partial u}{\partial t} = \frac{\partial u}{\partial x}, \quad \frac{\partial v}{\partial t} = -\frac{\partial v}{\partial x}, \quad (1)$$

to ensure the two populations “run” in the desired direction. To model the reversal of direction, we suppose the rate at which a left mover becomes a right mover is given by the *tumbling rate* function $r(u, v)$. A right moving agent is no different from a left moving agent beyond the direction of movement, so the tumbling rate for the right movers is that of the left movers, but with the concentrations exchanged, or simply $r(v, u)$. Then, the net exchange rate of left movers to right movers is given by $r(u, v) - r(v, u)$.

If we assume that tumbling events are uncorrelated and occur at a frequency μ , the tumbling rate becomes $r(u, v) = \mu u$. This yields a total concentration $\rho = u + v$ that adheres to a damped wave equation $\partial_t^2 \rho + 2\mu \partial_t \rho = \partial_x^2 \rho$. This hyperbolic equation, known as the Goldstein-Kac model or the telegrapher’s equation, has been shown to be the continuous limit of a random walk where particles move at a constant speed ± 1 and change direction at random times [9, 10]. While the myxobacteria may adhere to

the Goldstein-Kac model in some limiting cases, this equation has neither scientific accuracy (since we know tumbling events occur from local particle interactions), nor mathematically interesting spatial dynamics (since damped wave equations exhibit simple diffusive decay towards constant concentration profiles for large times). Moreover, we shall see later that even with nonlinear tumbling rates, the ODE describing stationary solutions reduces to a single first order equation. However, cluster shaped concentration profiles, which are shaped somewhat like a bell-curve, must have at least one critical point. So, run-and-tumble dynamics alone are insufficient in describing the formation of fruiting bodies.

To address this issue, we include diffusion of each population $\varepsilon^2 \partial_x^2 u$ and $\varepsilon^2 \partial_x^2 v$ according to the rate ε in the respective equations of u and v . Diffusion terms of this type have been shown to manifest from weak non-local interactions in particle based models [11]. In contrast, diffusion due to tumbling originates from random or local interactions. Alternatively, we can view this diffusive term as perturbation of the otherwise constant speed of propagation. Combining running, tumbling, and now diffusion, the full equation we consider is the reaction-transport-diffusion equation

$$\begin{aligned}\frac{\partial u}{\partial t} &= \varepsilon^2 \frac{\partial^2 u}{\partial x^2} + \frac{\partial u}{\partial x} - r(u, v) + r(v, u), \\ \frac{\partial v}{\partial t} &= \varepsilon^2 \frac{\partial^2 v}{\partial x^2} - \frac{\partial v}{\partial x} + r(u, v) - r(v, u).\end{aligned}\tag{2}$$

Predating work on myxobacteria, the first person to systematically study pattern formation through reaction-diffusion equations was Alan Turing, perhaps better known for his work in early computer science [12].

To then choose a tumbling rate, we assume that tumbling events are not triggered by collisions between agents moving in the same direction. Then, the frequency at which a left mover will change direction is given by $g(v)$, and the tumbling rate takes the form $r(u, v) = u \cdot g(v)$. Such tumbling rates ignore all but head-on collisions between the two populations—we use the term *head-on sensing* to refer to this class of tumbling rates. If we were to only consider binary collisions, we would have $g(v) = \alpha v$, in which case $r(u, v) = r(v, u)$, i.e. there is no net transfer between populations. Thus, to model the desired behavior, we must make a more sophisticated choice of g .

To accomplish this, Scheel and Stevens proposed the simple monotone tumbling frequency $g(v) = \mu + v^p / (1 + \gamma v^q)$ with positive parameters μ , γ , and $p \geq q$ [3]. Once again, the parameter μ gives the rate of spontaneous reversals of the bacteria. The nonlinear term should be thought of as an arbitrary power law v^p for low concentrations of v , and the power law v^{p-q} when v reaches a saturation concentration $\sqrt[p-q]{1/\gamma}$. In the case when $p = q$, the parameter γ roughly corresponds to the extent that collisions are uncorrelated, for large γ results in $r(u, v) \approx \mu u$. Our primary results

pertain to this tumbling rate of Scheel and Stevens where $p = q = 2$, i.e.

$$r(u, v) = u \left(\mu + \frac{v^2}{1 + \gamma v^2} \right). \quad (3)$$

Now having specified all aspects of our model, we wish to answer the following two questions:

Question 1. *Can myxobacteria clusters like the ones viewed in experiments exist within this model?*

Question 2. *If those clusters exist, are they dynamically as experiments suggest?*

In section 2, we use the techniques of rigorous mathematical analysis to study the properties and show the existence of clustering in this parameter regime. We show the existence of two families of stationary solutions: localized peaks (clusters) and troughs (gaps) for $\gamma < (4\mu + 8)^{-1}$ in an otherwise uniform background concentration. These families are uniquely determined by the total concentration far away—the background concentration. We establish these results analytically through a geometric analysis of a three-dimensional ordinary differential equation. Our argument uses perturbation theory to determine the local existence of these families near two critical solutions of uniform concentration. From here, we exploit the spatial reversal symmetry of this equation to get global existence. In addition, we consider solutions of two uniform concentrations that meet at a localized interface, which we refer to as a front solution. We found that if front solutions exist—and they do in certain parameter regimes—then the two families of cluster and gap type solutions limit on a unique front solution.

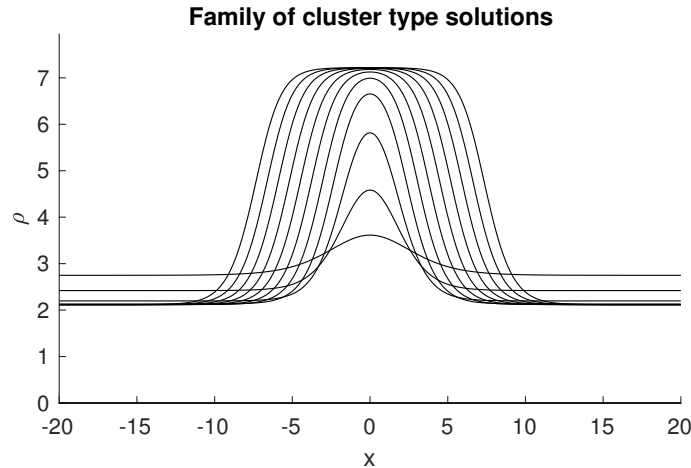


Figure 2: A sample of the results of a numerical continuation experiment used to compute a family of cluster type stationary solutions for $\gamma = 1/16$, with ρ denoting the total concentration $u + v$ and x denoting the spatial variable. By considering these solutions on the half domain, we observe convergence to a front.

We supplement this analysis with numerical solutions of cluster and gap type solutions. We describe these methods in section 3, and present the results of these computations with discussion in section 4. First, we implement numerical continuation code to find both families of solutions as a function of the background state. We observe that as the background concentration of the peak solutions lowers, the peak broadens to a plateau, and the width of these plateaus grows to infinity. See figure 2 for a sample of such a cluster computation. Our computations show convergence of the cluster solution to a front solution reflected about an arbitrary point. We found that the gaps converge to the same front type solution, albeit reflected in the opposite way.

To understand the stability of the clusters, gaps and fronts, we implement code to compute the spectrum of the PDE linearized about the numerical solutions from the continuation code. Specifically, we linearize the PDE about a profile to get a second order linear PDE with non-constant coefficients in x . Then, we look for solutions with ansatz $e^{\lambda t}(u(x), v(x))$ to this linearized equation. This gives us an eigenvalue problem, where eigenfunctions with $\text{Re}(\lambda) > 0$ correspond to unstable perturbations of the profile of interest. Upon discretizing our domain, this infinite dimensional eigenvalue problem becomes finite dimensional and amenable to computational methods. This numerical work suggests that cluster, gap and front solutions are generally stable for $\gamma \lesssim 1/16$. By combining this numerical and analytical work, we demonstrate how this minimalist model exhibits clustering behavior.

2 Mathematical analysis

Our theoretical results are central to motivating and understanding the significance of numerical results. We shall begin with three loosely stated results. These proofs use the technical language of mathematics out of necessity. However, the primary techniques are the analysis of ODE, perturbation, the use of upper bound estimates, and symmetry in 3-space, which should all be fairly familiar to physicists. Our results, stated informally, are:

Result 1. *When γ is sufficiently small, the model has a family of stationary solutions that represent spatially symmetric clusters of total bacterial concentration, as well as a family of stationary solutions that represent spatially symmetric gaps in bacterial concentration. In both cases, these solutions are uniquely determined (up to spatial translation) by the concentration at infinity, or background concentration.*

Result 2. *These two families of solutions can be thought of as single family, connected by a solution representing two different background concentrations meeting at an interface where the concentration increases or decreases suddenly in x over a small distance.*

In the language of dynamical systems, the clusters and gaps are *homoclinic*. Homoclinic solutions converge to a constant solution (i.e. equilibrium) in the limit

$|x| \rightarrow \infty$. The fronts are similar in that they limit on constant solutions for large $|x|$, but these solutions are different between $x = \infty$ and $x = -\infty$. Such solutions are called *heteroclinic*. In other words, homoclinic solutions begin and end at a single equilibrium solution, whereas heteroclinic solutions connect two different equilibria. Thus, we could restate results 1 and 2 as follows: there are two families of homoclinic solutions connected by a heteroclinic solution.

2.1 Observations for general tumbling rates

As noted in the introduction, our model adheres to a very strict symmetry by interchanging u with v and x with $-x$. Because this symmetry holds for general tumbling rates, we shall only assume that r is a smooth function. In this section, we exploit this symmetry to demonstrate that bounded stationary solutions to equation (2) must come in one of three flavors: homoclinic, heteroclinic, or periodic.

This restriction especially manifests for stationary solutions. Setting $m = u - v$, we can cast our problem in terms of the transformed coordinates (ρ, m) instead of (u, v) :

$$\begin{aligned}\frac{\partial \rho}{\partial t} &= \varepsilon^2 \frac{\partial^2 \rho}{\partial x^2} + \frac{\partial m}{\partial x}, \\ \frac{\partial m}{\partial t} &= \varepsilon^2 \frac{\partial^2 m}{\partial x^2} + \frac{\partial \rho}{\partial x} + mR(\rho, m).\end{aligned}\tag{4}$$

where we have defined the

$$R(\rho, m) = (-2r(u, v) + 2r(v, u))/m.\tag{5}$$

As an aside, observe that when spatial derivatives are small, we have

$$m(x, t) \sim m(0, x) \exp\left(\int_0^t R(\rho(x, t), m(x, t)) dt\right).\tag{6}$$

Hence, we can view R as a growth rate of the disparity between u and v . Since states that favor one population strongly over the other (i.e. $|m| \gg 0$) feature net movement of concentration, we expect that large and positive values of R should lead to instabilities in stationary solutions, while negative R should favor stability.

Note that $0 = m = u - v$ solves $r(u, v) - r(v, u) = 0$, so as long as r is smooth in each variable, we can smoothly extend the function $R(\rho, m) = (-2r(u, v) + 2r(v, u))/m$ to values where $m = 0$. So, we assume that R is sufficiently smooth everywhere on the plane $(\rho, m) \in \mathbb{R}^2$. Moreover, R is even in m , since exchange of u and v manifests as a sign change in m .

We first restrict our analysis to stationary solutions $\partial_t(\rho, m) = 0$. Then $\rho_x + m$ is equal to a constant, which we will call θ . Then, $m = \theta - \rho_x$, so we can refactor our

equation as a third-order ODE in ρ :

$$-\varepsilon^4 \rho''' + \rho' + (\theta - \varepsilon^2 \rho')R(\rho, \theta - \varepsilon^2 \rho') = 0. \quad (7)$$

where primes denote x derivatives. As mentioned in the introduction, we now see how the absence of diffusion leaves us with trivial stationary solutions. In the case $\varepsilon = 0$, our ODE becomes

$$\rho' = -\theta R(\rho, \theta). \quad (8)$$

Such first order equations are only capable of having constant, strictly increasing, or strictly decreasing solutions. This is in contradiction to the stationary clustering behavior we wish to model.

Throughout the remainder of this report, we shall only consider the case of $\varepsilon = 1$ and $\theta = 0$, giving the third order ODE

$$\rho''' = \rho'(1 - R(\rho, \rho')). \quad (9)$$

Alternatively, we can regard this third order equation as a system of three first order ODE by setting $\rho' = \sigma$ and $\rho'' = \tau$. This gives us the system

$$\frac{d}{dx} \begin{pmatrix} \rho \\ \sigma \\ \tau \end{pmatrix} = F \left(\begin{pmatrix} \rho \\ \sigma \\ \tau \end{pmatrix} \right) = \begin{pmatrix} 0 & 1 & 0 \\ 0 & 0 & 1 \\ 0 & 0 & 0 \end{pmatrix} \begin{pmatrix} \rho \\ \sigma \\ \tau \end{pmatrix} + \begin{pmatrix} 0 \\ 0 \\ (1 - R(\rho, \sigma))\sigma \end{pmatrix} \quad (10)$$

This equivalent form of the equation, though less convenient to write out, has two major advantages: first, now we can reason about solutions to equation (9) as curves or trajectories in 3d space. In decomposing this system into linear and nonlinear parts, we already get a sense of how the system behaves when linearized about a constant solution where $\sigma = \tau = 0$.

Observe that if $\rho(x)$ is a solution to equation (9), then $\rho(-x)$ is also a solution. This is a manifestation of the same symmetry outlined in the background, were we exchange u and v and negate x . We can state this symmetry another way, in view of the phase space of equation (10): define $S : \mathbb{R}^3 \rightarrow \mathbb{R}^3$ by $(x, y, z)^T \mapsto (x, -y, z)^T$. Then denote the plane of fixed points of S by $\text{Fix}(S) = \{(x, 0, z)^T \mid (x, z) \in \mathbb{R}^2\}$. Then if $\Psi = (\rho, \sigma, \tau)^T$ solves equation (10), we have that $S\Psi(-x)$ is also a solution. In other words, $\rho(x)$ is necessarily an even function about any critical point. Observe that any function that is even about at least two distinct points must be periodic. Thus, any $\rho(x)$ is either periodic, even about exactly one point, or is strictly increasing or decreasing. This gives us fairly strong information about the nature of bounded solutions. We summarize this information with a rigorous proof in the following Lemma.

Lemma 1. *A non-constant solution $\Psi = (\rho, \rho', \rho'')^T = (\rho, \sigma, \tau)^T$ to equation (10) cannot have more than two intersections in the fixed point subspace of S . The solution*

Ψ has two intersections if and only if it is periodic. If Ψ is bounded and not periodic, then it has zero intersections if and only if it is heteroclinic, and one intersection if and only if it is homoclinic.

Proof. Take Ψ to be any (possibly unbounded) non-equilibrium solution to equation (10). Then denote $\bar{\Psi} = (\bar{\rho}, \bar{\rho}', \bar{\rho}'')^T$ where $\bar{\Psi}(x) = S\Psi(-x)$. Then if $\Psi(x_0)$ intersects $\text{Fix}(S)$, it follows that $\Psi(x_0) = \bar{\Psi}(-x_0)$. By uniqueness of solutions, $\bar{\Psi}(x - x_0) = \Psi(x + x_0)$. Thus $\rho(x_0 - x) = \rho(x_0 + x)$, i.e. ρ is even about x_0 .

First suppose that Ψ intersects $\text{Fix}(S)$ at least twice. Then there exists $x_1 < x_2$ such that $\Psi(x) \in \text{Fix}(S)$ when $x \in \{x_1, x_2\}$ and $\Psi(x) \notin \text{Fix}(S)$ for $x \in (x_1, x_2)$. Since ρ is even about x_2 , we have that $(\rho(x_1), \rho'(x_1), \rho''(x_1))^T = (\rho(2x_2 - x_1), -\rho'(2x_2 - x_1), \rho''(2x_2 - x_1))^T$. Since $\rho'(x_1) = 0$, it follows that $\Psi(x + x_1) = \Psi(x + 2x_2 - x_1)$ for all x , thus showing periodicity. Furthermore, because $\rho'(x) > 0$ for all $x \in (x_1, x_2)$, it follows that $2(x_2 - x_1)$ is the smallest possible period. The converse trivially follows.

We now consider the case of bounded Ψ with less than two intersections with $\text{Fix}(S)$. Equivalently, ρ only has two critical points. Therefore the limits $\rho_\infty = \lim_{x \rightarrow \infty} \rho(x)$ and $\rho_{-\infty} = \lim_{x \rightarrow -\infty} \rho(x)$ exist, i.e. Ψ is either heteroclinic or homoclinic.

Consider the case of one intersection. Then ρ is even about some point, so $\rho_\infty = \rho_{-\infty}$. Conversely, if $\rho_\infty = \rho_{-\infty}$ and ρ had no critical points, then ρ is constant. Therefore, ρ must have one critical point.

When Ψ has zero intersections, ρ is strictly monotone in x . Thus $\rho_\infty \neq \rho_{-\infty}$. The converse follows from deduction. \square

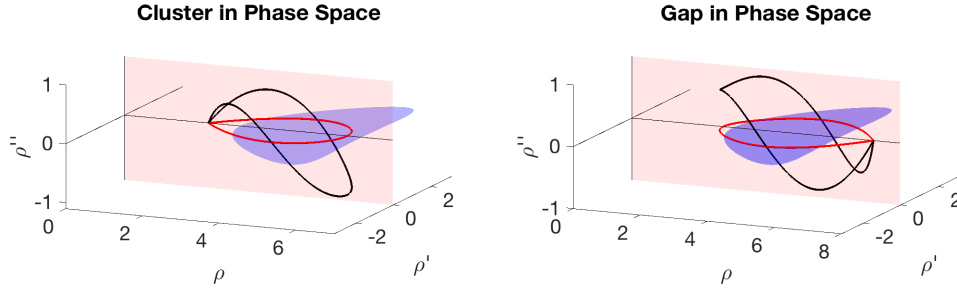


Figure 3: Homoclinic trajectories in phase space (black), their projections onto the ρ - ρ' plane (red) and the region G in the ρ - ρ' plane (blue) for $\gamma = 1/16$ and $\mu = 1$. The plane $\text{Fix}(S)$ is shown in pink. See Section 4.1 for details on how these solutions were found numerically.

2.2 Head-on sensing

We now limit our analysis to the tumbling rate described in the introduction, $r(u, v) = u(\mu + v^2/(1 + \gamma v^2))$. If an explicit integral to equation (9) exists with this tumbling rate, we do not know it. Despite this, the system still respects the symmetry outlined in the previous section 2.1 and Lemma 1.

We compute R explicitly with this tumbling rate

$$R(\rho, m) = -2\mu + 2 \frac{4(\rho^2 - m^2) - \gamma(\rho^2 - m^2)^2}{16 + 8\gamma(\rho^2 + m^2) + \gamma^2(\rho^2 - m^2)^2}. \quad (11)$$

Now that we have a particular definition for R , we again consider the equation (9). We use the coordinates $(\rho, \sigma, \tau)^T$ when considering solutions as trajectories in phase space. Equilibrium for equation (10) exist on the line $(\rho, \sigma, \tau)^T \in \text{span}((1, 0, 0)^T)$. Linearizing about such a constant equilibrium solution $\rho(x) = \rho_\infty$, the Jacobian matrix is

$$J = \begin{pmatrix} 0 & 1 & 0 \\ 0 & 0 & 1 \\ 0 & 1 - R(\rho_\infty, 0) & 0 \end{pmatrix} \quad (12)$$

For $\gamma < \gamma^* := (4 + 8\mu)^{-1}$, $R(\rho_\infty, 0) - 1$ has only two positive roots ρ_\pm . These are given by the formula

$$\rho_\pm^2 = 4 \frac{1 - \gamma - 2\gamma\mu \pm \sqrt{1 - 4\gamma - 8\gamma\mu}}{2\gamma + \gamma^2 + 2\gamma^2\mu}. \quad (13)$$

Importantly, $R(\rho, 0)$ is positive within (ρ_-, ρ_+) , and negative for all other values of $\rho > 0$. This amounts to J having eigenvalues $0, \eta$, and $-\eta$ where η is imaginary when $\rho \in (\rho_-, \rho_+)$ and real otherwise.

The special case of $\rho = \rho_\pm$ leaves us with a degenerate Jacobian with eigenvalue 0 repeated thrice. At these points, the we lose the existence of stable or unstable manifolds and higher order nonlinear terms of the Taylor expansion of R become significant in the context of perturbation. The leading order happens to be $(\rho - \rho_\pm)^2 \sigma$, for which we can compute explicit homoclinic solutions. To make analysis of this Taylor expansion rigorous, we rescale ρ and x by powers of a constant ϵ in a way that gives us only the leading order term when we set $\epsilon = 0$. Then, by showing that these homoclinic solutions persist for small $\epsilon > 0$, we can undo the rescaling and conclude that small homoclinic solutions for equilibria near ρ_\pm exist. However, generally perturbative arguments like these can only explain the behavior of the ODE on small intervals, whereas a solution being homoclinic is a statement about the ODE on the whole domain. To get the desired global result, we utilize the implicit function Theorem (see Appendix), the reflective symmetry of the ODE, and a technical result regarding the smoothness of stable manifolds in parameters due to Hale [13]. The result, with its rigorous proof, is as follows:

Theorem 1. *There exist two families of homoclinics for equation (9) when $\gamma > 0$ is sufficiently small. Specifically, for $\delta > 0$ small enough, the equilibrium $(\rho, \sigma, \tau)^T = (\rho_\pm \pm \delta, 0, 0)^T$ has a homoclinic orbit.*

Proof. The proof for homoclinics near ρ_- is nearly identical to that of ρ_+ . For this reason, we omit the proof for ρ_- .

Since R is locally analytic everywhere in \mathbb{R}^3 , we use its Taylor expansion about $(\rho, \rho') = (\rho_+, 0)$:

$$\rho'(R(\rho, \rho') - 1) = \alpha_{1,0}(\rho - \rho_+)\rho' + \sum_{j \geq 2, k \geq 0} \alpha_{j,k}(\rho - \rho_+)^j(\rho')^{2k+1}. \quad (14)$$

We have omitted some terms, exploiting the fact that R is even in ρ' . Importantly, $\alpha_{1,0} = \partial_a(1 - R(a, 0)|_{a=\rho_+}) > 0$ and so $(\rho, \rho', \rho'')^T = (\rho_+ + \delta, 0, 0)^T$ gives a hyperbolic equilibrium. We then set $\epsilon\psi(\sqrt{\epsilon\alpha_{1,0}}x) = \rho(x) - \rho_+$ for any $\epsilon > 0$. We shall denote our new spatial variable $\xi = \sqrt{\epsilon\alpha_{1,0}}x$. Under this change of variables, only the lowest order term survives in the limit $\epsilon \rightarrow 0$:

$$\begin{aligned} \epsilon^{5/2}\alpha_{1,0}^{3/2}\psi''' &= \epsilon^{5/2}\alpha_{1,0}^{3/2}\psi\psi' + \sum_{j \geq 2, k \geq 0} \alpha_{j,k}\epsilon^{j+3k+3/2}\alpha_{0,1}^{k+1/2}\psi^j(\psi')^{2k+1} \\ \Leftrightarrow \psi''' &= \psi\psi' + \sum_{j \geq 2, k \geq 0} \alpha_{j,k}\epsilon^{j+3k-1}\alpha_{0,1}^{k-1}\psi^j(\psi')^{2k+1} = \psi\psi' + O(\epsilon) \end{aligned} \quad (15)$$

Formally, we set $\epsilon = 0$ to get a truncated equation $\psi''' = \psi\psi'$, for which unique homoclinic orbits exist for each equilibrium along the line $\text{span}(1, 0, 0)^T$ in phase space. These solutions have the explicit form

$$\psi(\xi) = \psi_\infty(1 - 3\text{sech}^2(\psi_\infty^{1/2}\xi/2)) \quad (16)$$

where $\lim_{|\xi| \rightarrow \infty} \psi(\xi) = \psi_\infty > 0$. We shall show that homoclinic orbits exist within some neighborhood of $\epsilon = 0$, so that our change of variables is well-defined.

Using the Stable Manifold Theorem, we have that $(\psi_\infty, 0, 0)^T$ has an unstable manifold that varies smoothly (at least continuously differentiable) in ϵ [13]. We regard this manifold $W^u(\epsilon)$ as a curve $c(\epsilon, q)$ in \mathbb{R}^3 , continuously differentiable both in ϵ and a parameter $q \in \mathbb{R}$. Define $F((q, r, s); \epsilon) = c(q; \epsilon) - (r, 0, s)$. We know $W^u(0)$ intersects the plane $\text{Fix}(S)$ transversely. Hence there exists (q_0, r_0, s_0) for which F vanishes and has a nonsingular Jacobian. Then, by the implicit function theorem, there exists a neighborhood of $\epsilon = 0$ such that we write $q = q(\epsilon)$ where $c(\epsilon, q(\epsilon))$ intersects $\text{Fix}(S)$ transversely. By taking this neighborhood to a subset neighborhood, we ensure that $c(q; \epsilon)$ does not intersect at the axis of equilibria. Thus, trajectories in this branch of $W^u(\epsilon)$ shall not converge to another equilibrium, and must pass transversely through $\text{Fix}(S)$. As equation (15) respects the same symmetry as equation (9), we have that $\lim_{|\xi| \rightarrow \infty} \Phi(q(\epsilon), \xi) = (\psi_\infty, 0, 0)^T$. \square

Hereafter, we shall refer to the homoclinic solutions with a global minimum as “gaps” and those with a global maximum as “clusters.” As shown in Section 2.1, the symmetry $(x, u, v) \mapsto (-x, v, u)$ vastly restricts the complexity of spatial dynamics. By considering the concavity of the homoclinics and the nature of the nonlinearity, we deduce further restrictions. We define $G = \{(a, b)^T \mid R(a, b) > 1, a > 0\}$. Then if $\rho > 0$, we have that $(\rho(x), \rho'(x)) \in G$ if and only if $\text{sgn}(\rho'''(x)) = -\text{sgn}(\rho'(x))$. Then

any local maximum of $\rho'(x)$ must occur when $\Psi(x) \in G \times \{0\}$. We present a cluster and gap solution as a trajectory in phase space together with the region G in figure 3 for $\gamma = 1/16$ and $\mu = 1$.

Lemma 2. *Let $0 < \gamma < \gamma^*$. Then the set of bump solutions with equilibria in $[0, \rho_-)$ has bounded and continuous first, second and third derivatives (i.e. $\rho \in C^3(\mathbb{R})$) independently of ρ_∞ .*

Proof. Observe that $-2\mu - 2/\gamma \leq R(a, b) \leq -2\mu + 1/\gamma$ for all a, b . We define $M := 2(\mu + 1/\gamma)$ to get the bound $|1 - R| \leq M$. By computing $\partial G = \{(a, b)^T \mid R(a, b) = 1\}$, the reader will also find that G is bounded.

Now, set $\rho(x)$ to be a cluster solution to the equilibrium ρ_∞ . We first show that ρ' is bounded. Before ρ attains its maximum, it has an inflection point at $x_i < 0$. Then $\rho'''(x_i) < 0$, so $(\rho, \rho')^T(x_i)$ lies in the bounded open set \cdot . Take $K > 0$ such that $G \subseteq [-K, K]^2$. Since $\rho'(x_i)$ is the maximum value of ρ' , it follows that $\rho' \leq K$ for all ρ_∞ . The symmetry requires that $\max_{x \in \mathbb{R}} \rho'(x) = -(\min_{x \in \mathbb{R}} \rho'(x))$, so $\rho' \geq -K$. This implies that $|\rho''| < KM$.

The bound $|\rho''(x)| \leq M(\rho(x) - \rho_\infty)$ implies that if $\rho(x)$ is bounded from above, then ρ'' is also bounded. To show ρ is bounded from above, we argue by contradiction: suppose there was a homoclinic for which ρ exceeds any arbitrary N . In particular, $\rho(x) > N$ for all x in some ball $B(0, x_N)$. In the limit $a \rightarrow \infty$ when b is bounded, $R(a, b) \rightarrow -2\mu - 2/\gamma$. Hence, taking N to be large enough, we have that $\rho'''(x) > (1 + 2\mu + 2/\gamma - 1/2)\rho'(x)$ for all $x \in (-x_N, 0)$. Define $C_\gamma = 1/2 + 2(\mu + 1/\gamma)$. We exploit our assumption further to find solutions for which $\rho(0) > \alpha N$ and $\rho(-x_N) = N$ for any $\alpha > 1$. Then $\rho''(0) - \rho''(-x_N) > C_\gamma(\alpha - 1)N$. Moreover, $\rho''(-x_N) > -M(N - \rho_\infty) > -MN$. Then $\rho''(0) > C_\gamma(\alpha - 1)N - MN$. Then, by taking $\alpha > (C_\gamma + M)/C_\gamma$, we get $\rho''(0) > 0$, which is a contradiction. Thus ρ is bounded from above, which implies ρ'' is bounded from below. In summary, ρ , ρ' , ρ'' and ρ''' all have bounds independent on ρ_∞ . \square

Theorem 2. *Let S be the set of all equilibria in $(0, \rho_\infty)$ with cluster solutions. Then if $\rho_-^* \in (\partial S) \setminus \{\rho_-\}$, there exist two positive heteroclinic solutions $\rho^*(x)$ and $\rho^*(-x)$ connecting equilibria ρ_-^* to $\rho_+^* \in [\rho_+, \infty)$.*

Proof. Since ρ_-^* lies in $(-\rho_-, \rho_-)$, it has an unstable manifold. Let $\rho^*(x)$ be a solution along the unstable manifold such that $\lim_{x \rightarrow -\infty} (\rho^*)'(x) > 0$. Then, $\rho_\infty \in (\rho_-^*, b)$ have a cluster $\rho(x)$ with $\rho'(0) = 0$. We have that the unstable subspaces for the linearization about equilibria in $(0, \rho_-)$ vary smoothly in ρ_∞ within a neighborhood of $(\rho_-^*, 0, 0)^T$ in phase space; we use this fact, along with smoothness on initial conditions, to get the following continuity result: For any $x_f < 0$ and $\epsilon > 0$, there exists an x_0 and $\delta > 0$ such that for all $\rho_\infty \in B(\rho_-^*, \delta)$, $\|\rho^*(x) - \rho(x - x_0)\|_{C^2(-\infty, x_f]} < \epsilon$. Thus, by the preceding Theorem, it follows that ρ^* is also bounded. But, ρ^* is neither periodic nor homoclinic, so it must be heteroclinic. Moreover, $\rho^*(x)$ must have at least one point of inflection. One can show that $G \subseteq (\rho_-, \infty) \times \mathbb{R}$. Thus $\rho^*(x) > \rho_-$ for all

x large enough. Since $\lim_{x \rightarrow \infty} \rho^*(x)$ cannot be a elliptic equilibrium, we have that $\lim_{x \rightarrow \infty} \rho^*(x) \geq \rho_+$. \square

Loosely, this Theorem states that “homoclinics limit on heteroclinics as one varies the background state ρ_∞ .” This observation forms the basis for the numerical continuations of Section 4. This corollary also gives us a sufficient condition for the existence of a heteroclinic: choose $\rho_-^* \geq 0$ such that ρ_∞ has a cluster for all $\rho_\infty \in (\rho_-^*, \rho_-)$. Then if we choose ρ_-^* to be as small as possible, ρ_-^* has heteroclinic solutions.

This corollary begs the question of the existence of heteroclinics. Showing their existence for all $0 < \gamma < \gamma^*$ will require a more delicate argument than presented here, but we show their existence for γ bounded away from zero. To do this, it suffices to show that the largest interval (ρ_-^*, ρ_-) for which all $\rho_\infty \in (\rho_-^*, \rho_-)$ is bounded away from $-\rho_-$ (and ideally nonnegative in view ρ representing a concentration).

First, while this system has no obvious first integral, we do have what one might call an approximate first integral. Take any function $Q(\rho)$ such that $Q(\rho) \geq R(\rho, \rho')$ for all ρ, ρ' . Then if $\rho(x) \rightarrow \rho_\infty$ as $x \rightarrow -\infty$ and ρ is strictly increasing on $x \leq x_f$, we have $\rho'' \geq \int_{\rho_\infty}^{\rho} 1 - Q(a) da$ for all $x \in (-\infty, x_f)$. Multiplying by ρ' and integrating in ρ once more, we get an explicit bound on ρ' :

$$\rho' \geq \sqrt{2 \int_{\rho_\infty}^{\rho} \int_{\rho_\infty}^b 1 - Q(a) da db} =: q(\rho) \quad (17)$$

Thus, if $G \subseteq \{(a, b)^T \mid |b| \leq q(\rho), a > \rho_\infty\} =: B$, then $(\rho, \rho')^T$ never enters G and so $\rho''' > 0$ for all $x < x_f$. In such a case, $\rho''(x_f)$ is never zero. This implies $\rho''(x) > 0$ for all x where ρ is defined, and likewise for ρ' . Thus $\rho(x) \rightarrow \infty$ in finite or infinite x .

To get nonnegative solutions, we set $\rho_\infty = 0$. The simplest nontrivial candidate for an upper bound Q is

$$Q(\rho) = -2\mu + \rho^2/(2 + \gamma\rho^2). \quad (18)$$

Although we can use more sophisticated bounds using local maxima of R , this approach affords no great advantage over the bound (18) once γ becomes small. The full computation of $q(\rho)$ is

$$q(\rho) = \frac{1}{\gamma} \sqrt{\rho^2(2\gamma^2\mu + \gamma^2 - \gamma) + 2 \log \left(\frac{2}{\gamma\rho^2 + 2} \right) + 2\sqrt{2\gamma}\rho \arctan \left(\sqrt{\frac{\gamma}{2}}\rho \right)}. \quad (19)$$

Meanwhile, $\bar{m}(\rho) := \sup\{m \mid (\rho, m) \in G\}$ is given by

$$\bar{m}(\rho) = \sqrt{\rho^2 - \frac{4(2\mu + \gamma + 1) - 4\sqrt{1 - \gamma^3(2\mu\rho + \rho)^2 - 2\gamma^2(2\mu + 1)\rho^2}}{2\gamma^2\mu + \gamma^2 + 2\gamma}}. \quad (20)$$

We show a sample of plots of the the regions G and B for a few values of γ and $\mu = 1$. Our plots suggest that $B \subseteq G$ whenever $\gamma \in (\gamma_0, 1/12)$, where $\gamma_0 \in (1/18, 1/17)$. For all smaller γ , we found that $G \not\subseteq E$. This is not surprising: when $\gamma = 0$, G is unbounded, yet B is bounded.

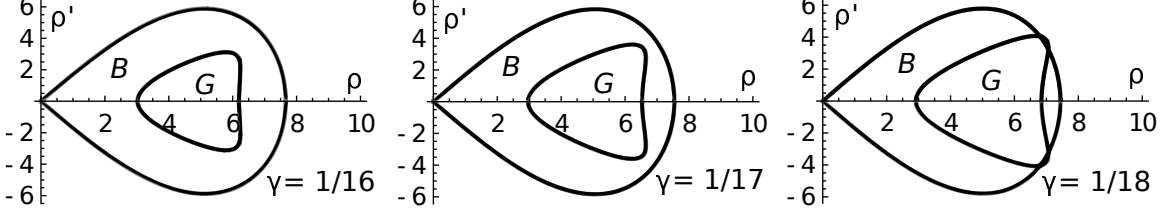


Figure 4: Plot of the boundaries of B and G in the ρ - ρ' plane for $\mu = 1$.

To complement this graphical argument, we provide a more rigorous (but less explicit or geometric) argument for the existence of heteroclinics when $\gamma < \gamma^*$ is in a neighborhood of γ^* . Once again we prove the existence of unbounded increasing solutions along the unstable manifolds of equilibria $\rho_\infty \in [0, \rho_-)$. Take $\rho(x)$ to be an unstable solution to ρ_∞ with $\rho' > 0$ for all sufficiently negative x . This solution is unique up to translation in x . As the region G is empty for $\gamma \geq \gamma^*$, $\rho(x)$ is necessarily increasing and concave up for all x . Thus, for such γ , ρ is unbounded. Then take $\gamma_1 \in (0, \gamma^*)$. Choose an equilibrium such that $0 \geq \rho_\infty < \inf_{\gamma_1 \leq \gamma \leq \gamma^*} \rho_-$. Next, set $\bar{a} = \sup\{a \mid (a, b) \in G, \gamma_1 \leq \gamma \leq \gamma^*\}$, i.e. a right bound on G in the plane for all $\gamma \in (\gamma_1, \gamma^*)$. We have that $\rho(x) > 2\bar{a}$ for all sufficiently large x . Since the flow is continuous in γ , there exists a $\gamma_2 \in (\gamma_1, \gamma^*)$ such that $(\rho, \rho', \rho'')^T$ enters a compact subset of $(\bar{a}, \infty) \times \mathbb{R}_+ \times \mathbb{R}_+$ for all $\gamma \in (\gamma_2, \gamma^*)$. This implies that ρ has positive first, second and third derivatives for all later x , giving unboundedness.

3 Numerical Methods

Although we found existence of families of cluster and gap solutions, as well as partial existence of front solutions in Section 2.2, these purely theoretical results only paint a vague picture of the geometry of these types of solutions. Moreover, we do not report any results on stability of such solutions in the present paper. So, we use numerical tools to analyze the homoclinic and heteroclinic solutions. We use numerical continuation in two different contexts, as described in Section 3.1: first, to compute families of clusters and gaps for fixed γ in the limit as the background concentration ρ_∞ approaches that of a front; second, to compute fronts in the limit $\gamma \rightarrow 0$. In Section 3.4, we describe how we solve the eigenvalue problem of determining stable and unstable modes of equation 2 linearized about the concentration profile of interest. In Section 3.5, we describe how we further demonstrate the stability of solutions by applying small perturbations of the eigenmode with the largest growth rate.

3.1 Numerical continuation

To find cluster solutions numerically, we use numerical continuation methods. In short, numerical continuation is a method to solve the following problem: suppose we have a function $f_c : \mathbb{R}^n \rightarrow \mathbb{R}^n$ with the family of solutions U_c to the equation

$$f_c(U_c) = 0. \quad (21)$$

If we knew U_c for some c , we wish to find a $U_{c'}$ for c near c' , then a single iteration of Newton's method would give us a reasonable guess

$$U_{c'} \approx U_c - (Df_c)^{-1} f_{c'}(U_c). \quad (22)$$

Then, to find solutions U_c for a range of $c \in (a, b)$, we can use this method by starting with a , and incrementing c a small amount iteratively through the interval (a, b) , computing U_c at each step using Newton's method. Specifically, given a sequence of parameter values $c_k = a + \delta k$ with δ small, we compute the U_{c_n} iteratively by $U_{c_{n+1}} = U_{c_n} - (Df_{c_n})^{-1} f_{c_{n+1}}(U_{c_n})$. We use two different variations of this algorithm in the continuations of homoclinic and heteroclinic solutions to the ODE.

3.2 Homoclinic continuation

We begin with a constant stationary solution ρ_{\pm} given by equation (13). Using equation (14), we see that if we assume ρ' is small and ρ is sufficiently close to ρ_{\pm} , then this equation admits the approximation

$$\rho''' = \rho'(1 - R(\rho, \rho')) \approx -\alpha_{1,0}(\rho - \rho_{\pm})\rho'. \quad (23)$$

Hence, after translating ρ and rescaling x in the same way as in the proof of Theorem 1 (with $\varepsilon = 1$), we expect that ρ is approximated by (16) when ψ_{∞} is small. This constant $\alpha_{1,0}$ can be easily estimated, since it is just the partial derivative $\partial_{\rho} R(\rho, \rho')$ evaluated at $(\rho, \rho') = (\rho_{\pm}, 0)$. This should give us a good initial guess for a member of the family of cluster or gap solutions, that is, solutions near ρ_+ gives us gap type solutions, and solutions near ρ_- give us cluster type solutions.

Using this explicit approximation for a homoclinic cluster or gap type solution, we use a continuation method to compute solutions (ρ, σ, τ) of equation (10) with the background concentration $c = \rho_{\infty}$ as our parameter. We compute the homoclinic profiles on the spatial domain $[0, L]$, where L is sufficiently large and the unique extreme value of the homoclinic is located at $x = 0$. At $x = L$, we want the homoclinic solution to behave like a solution close to the hyperbolic equilibrium $(\rho_{\infty}, 0, 0)$. To do this, we linearize equation (10) about $(\rho_{\infty}, 0, 0)$ to get the Jacobian matrix of equation (12). Then (in view of the Stable Manifold Theorem), $(\rho - \rho_{\infty}, \sigma, \tau)$ should asymptotically approach the stable subspace of the ODE $\mathbf{u}'(x) = J\mathbf{u}(x)$ as $x \rightarrow \infty$. In practice, this means $(\rho(x), \sigma(x), \tau(x))$ approaches $(\rho_{\infty}, 0, 0) + e^{-\lambda x} \mathbf{u}_{\lambda}$ as $x \rightarrow \infty$,

where $\lambda > 0$ and \mathbf{u}_λ is some eigenvector satisfying $J\mathbf{u}_\lambda = -\lambda\mathbf{u}_\lambda$. Then, the projection of the normalized $(\rho(x), \sigma(x), \tau(x)) - (\rho_\infty, 0, 0)^T$ onto the orthogonal complement of $\text{span}(\mathbf{u}_\lambda)$ should be approximately 0. To ensure that our solution has this asymptotic property, we employ the (often neglected) linear algebra fact that the subspace $(\text{span}(\mathbf{u}_\lambda))^\perp$ is generated by the left eigenvectors of J with eigenvalue not equal to λ . Thus, after computing the two left eigenvectors \mathbf{v} and \mathbf{w} with eigenvalue not equal to λ , we set our right boundary conditions

$$\begin{aligned}\langle \mathbf{v}, (\rho(L) - \rho_\infty, \tau(L), \sigma(L)) \rangle &= 0 \\ \langle \mathbf{w}, (\rho(L) - \rho_\infty, \tau(L), \sigma(L)) \rangle &= 0.\end{aligned}\tag{24}$$

As long as L is taken to be large, these three boundary conditions will admit solutions that approach the equilibrium ρ_∞ for large x . Since we know ρ is even about any extreme value (in our case, ρ at $x = 0$), we easily extend (ρ, σ, τ) to values of x in $[-L, 0]$ to get a homoclinic solution.

Using a sufficiently small grid size $\delta x = L/N$, we approximate solutions (ρ, σ, τ) on the grid $\{0, \delta x, 2\delta x, \dots, N\delta x\}$. We shall use the vectors $\mathbf{r} = (r_0, \dots, r_N)^T$, $\mathbf{s} = (s_0, \dots, s_N)^T$ and $\mathbf{t} = (t_0, \dots, t_N)^T$, where r_k , s_k , t_k approximate of $\rho(k\delta x)$, $\sigma(k\delta x)$ and $\tau(k\delta x)$ respectively. We then define a function $f_c : \mathbb{R}^{3(N+1)} \rightarrow \mathbb{R}^{3(N+1)}$ such that our approximation $U_c = (\mathbf{r}, \mathbf{s}, \mathbf{t})^T$ is valid according to the differential equation (10) and the boundary conditions described earlier.

We use the trapezoidal rule finite difference scheme. To do this, we define two $N \times (N+1)$ matrices M and D :

$$M = \frac{1}{2} \begin{pmatrix} 1 & 1 & 0 & 0 & \dots & 0 \\ 0 & 1 & 1 & 0 & \dots & 0 \\ \vdots & & & \ddots & & \vdots \\ 0 & \dots & 0 & 0 & 1 & 1 \end{pmatrix}; D = \begin{pmatrix} -1 & 1 & 0 & 0 & \dots & 0 \\ 0 & -1 & 1 & 0 & \dots & 0 \\ \vdots & & & \ddots & & \vdots \\ 0 & \dots & 0 & 0 & -1 & 1 \end{pmatrix}.\tag{25}$$

In other words, M gives you the mean of two adjacent elements of a vector, whereas D gives you the difference. Then we define the first $3N$ components of f_c by concatenating the three vectors

$$\begin{aligned}M\mathbf{s} - (\delta x)^{-1}D\mathbf{r}, \\ M\mathbf{t} - (\delta x)^{-1}D\mathbf{s}, \\ M(s_0(1 - R(r_0, s_0)), \dots, s_N(1 - R(r_N, s_N)))^T - (\delta x)^{-1}D\mathbf{t}.\end{aligned}\tag{26}$$

The remaining three components of f_c are functions that equal 0 when the boundary conditions are satisfied. To ensure the first derivative of our approximation of ρ is zero, we set one of these remaining components to $f_c^{3N+1} = s_0$. After computing the 3-vectors \mathbf{v} , \mathbf{w} , the left eigenvectors of J with nonnegative eigenvalue, the right

boundary conditions are

$$\begin{aligned} f_c^{3N+2} &= \langle \mathbf{v}, (r_N - c, s_N, t_N)^T \rangle, \\ f_c^{3N+3} &= \langle \mathbf{w}, (r_N - c, s_N, t_N)^T \rangle. \end{aligned} \tag{27}$$

where we recall that $c = \rho_\infty$ is the desired value of ρ at infinity. This completes our definition of f_c^{3N+3} .

The most rudimentary form of continuation described at the beginning of this section is insufficient for this problem. Specifically, Df_c quickly becomes singular as c approaches the background equilibrium of a heteroclinic profile, meaning small changes in c result in large changes of the solution U_c . To circumvent this issue, rather than try to find curves parametrized by ρ_∞ , we instead try to find a parametrized curve $(c(s), U(s))$ for which $H(c(s), U(s)) := f_{c(s)}(U(s)) = 0$ at each point; now we have a function $H : \mathbb{R}^{N+1} \rightarrow \mathbb{R}^N$ which has full rank, and so $H^{-1}(0)$ should be a regular curve. This way, the family of solutions U does not need to be in one-to-one correspondence with the parameter c . The reader can find a description of this algorithm, due to Herbert Keller [14], in the context of boundary value problems in [15].

3.3 Heteroclinic continuation

Now, we take the limiting heteroclinic object of the family of homoclinic solutions computed from the continuation of 3.3 on the half domain $[0, L]$. Now, we want to compute these heteroclinics in the limit of $\gamma \rightarrow 0$. To do this, we want to allow the right and left boundary conditions to vary in γ as to preserve the heteroclinic structure. To do this, we define $f_\gamma : \mathbb{R}^{3N+5} \rightarrow \mathbb{R}^{3N+5}$. This function takes as arguments are the same $(\mathbf{r}, \mathbf{s}, \mathbf{t})$ as in the previous section, plus two additional numbers $\rho_{-\infty}$ and ρ_∞ that define the two equilibria we want the heteroclinic solution to converge to on the left and right respectively. The first $3N$ components of f_γ are given by the finite differences in equation (26). Now, we use the same finite difference scheme to define the first $3N$ components of f_γ . The next four components are defined by the projection boundary conditions described in the previous section. The final condition is the phase condition that $\langle \mathbf{s}_{\text{old}}, \mathbf{r} - \mathbf{r}_{\text{old}} \rangle = 0$, where \mathbf{r}_{old} and \mathbf{s}_{old} are the values of \mathbf{r} and \mathbf{s} from the previous computation, respectively. This condition constrains the degree of freedom induced by the translational symmetry of the ordinary differential. In other words, continuation will only change the shape of the front, and not translate it. For this method, we apply the Newton-Euler method described in section 2 of [16]. We choose values of γ that give $\sqrt{1/\gamma}$ on a uniform grid.

3.4 Linear stability eigenvalue problem

Having collected a variety of cluster, gap and front type solutions, we then use numerics to determine their stability, or whether or not they will persist under small perturbations. To determine the linear stability of the homoclinic and heteroclinic profiles, we linearize equation (2) about such a stationary solution $(u_0(x), v_0(x))$ and consider the effect of a small perturbation $e^{\lambda t}(u(x), v(x))$ that grows or decays exponentially in time according to the rate λ . The linearized equation, after dividing out $e^{\lambda t}$, is

$$\begin{aligned}\lambda u &= \frac{\partial^2 u}{\partial x^2} + \frac{\partial u}{\partial x} - n_u(x)u + n_v(x)v, \\ \lambda v &= \frac{\partial^2 v}{\partial x^2} - \frac{\partial v}{\partial x} + n_u(x)u - n_v(x)v\end{aligned}\tag{28}$$

where we defined

$$n_u = \frac{\partial}{\partial u}(r(u, v) - r(v, u))|_{(u,v)=(u_0,v_0)} \text{ and } n_v = \frac{\partial}{\partial v}(r(v, u) - r(u, v))|_{(u,v)=(u_0,v_0)}.\tag{29}$$

We use periodic boundary conditions on discretization of $[-L, L]$ with L taken to be sufficiently large. We use centered finite differences for first and second derivatives. Then, equation (28) can become matrix eigenvalue equation $A(\mathbf{u}, \mathbf{v}) = \lambda(\mathbf{u}, \mathbf{v})$ where A is a sparse matrix and \mathbf{u}, \mathbf{v} are the discretizations of $u(x), v(x)$ respectively. Using MATLAB's `eigs` function, we compute the eigenvalues and eigenfunctions of this problem for several points along the continuations of homoclinics and heteroclinics.

3.5 Direct simulation

Using the eigenvalue and eigenfunction data from stability computations, we further analyze time stability through direct simulation in time. We reflect the homoclinic or heteroclinic type solution about $x = 0$ to get an even stationary solution on the domain $[-L, L]$. For our initial data, we apply a small perturbations to this profile by its eigenfunction with largest $\text{Re}(\lambda)$ from the linear stability computation. We use MATLAB's `ode15s` to perform numerical time integration of the original PDE (2) on a discretized spatial domain to solve the initial value problem. We use upwind and downwind finite differences for first spatial derivatives of v and u respectively, and the centered finite difference for second spatial derivatives.

4 Numerical results & discussion

To summarize this study so far, in section 2, we developed the theoretical understanding of the run-and-tumble model as it pertains to the existence of stationary clusters. We show the existence of these homoclinic positive bump solutions, which we hypothesize correspond to the fruiting bodies formed by the myxobacteria. We

also prove existence of gap and front type solutions. In section 3, we describe the methods we use to find these solutions numerically, spanning continuation, solutions to eigenvalue and eigenvector problems, and solving the initial value problem of the PDE of interest. For all computations, we fix $\mu = 1$. With the exception of the continuation of heteroclinics in the limit $\gamma \rightarrow 0$, we use the parameters $\gamma = 1/16$, $\gamma = 1/64$ and $\gamma = 1/256$. For spatial plots of concentration profiles, we plot u in blue, v in red and ρ in black.

In subsection 4.1, we provide the samples from the homoclinic continuation computations, both as graphs of the concentrations u, v and ρ versus x , and as curves $(\rho(x), \rho'(x), \rho''(x)) = (\rho(x), \sigma(x), \tau(x))$ existing in 3D space. In subsection 4.2, we show the result of continuation of a front solution in the limit $\gamma \rightarrow 0$. In subsection 4.3, we show the results of linear stability computations on cluster, gap and front solutions found numerically from the continuations. Finally, in 4.4, we test this linear stability with direct simulation by computing the time evolution of profiles perturbed by eigenfunctions with largest growth rates. We discuss implications of numerical results in subsection 4.5

4.1 Homoclinic continuation

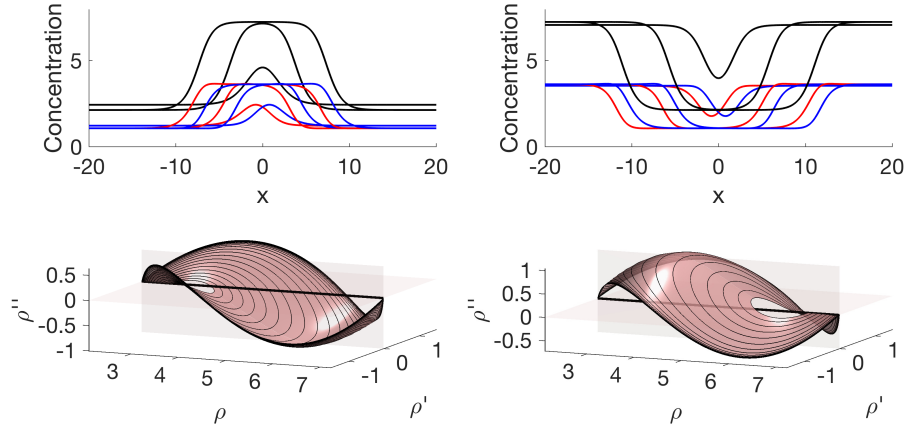
In figure 5, the reader will find samples of results from the continuation of homoclinic solutions in the background concentration for the parameter values $\gamma = 1/16, 1/64$ and $1/256$ respectively. Below the plots of ρ vs. x , the reader will find corresponding plots of the trajectories of these solutions in the phase space of equation (10). We can regard the collection of all these families as a parametrized surface in the variables ρ_∞ and x .

Taller and broader peaks correspond to solutions that had been computed later in the continuation. The flat and broad peak most easily seen in the later computations is characteristic of the front type solution. In later continuations, the background concentration becomes fixed. Instead, we see the broadening of the gaps and troughs.

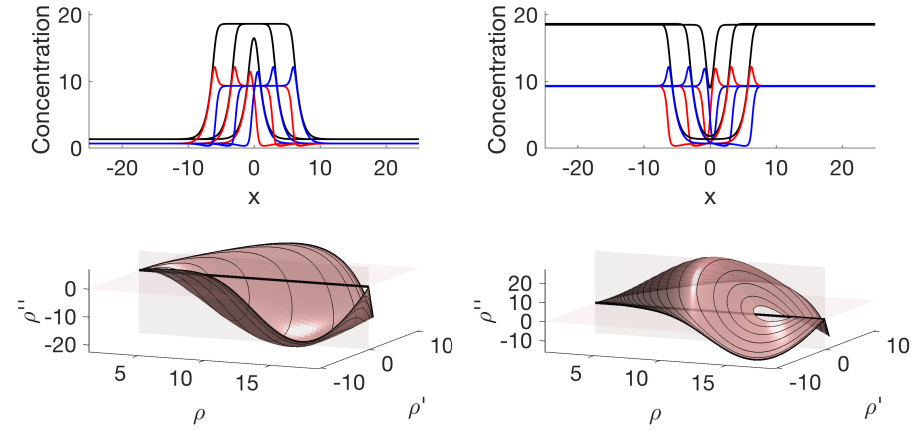
In the bottom four plots of figure 5, we observe convergence to front-like solutions, with broad flat regions meeting at steep interface. In the phase plots, we see the corresponding behavior. The final iterations of the continuation appear at the boundary of the surface. Rather than having the geometry characteristic of homoclinic solutions, i.e. a smooth closed loop that connects with itself at a single equilibrium, the later iterations more closely resemble heteroclinic solutions, with open curves connecting two different equilibria.

In figure 6, we use the continuation data to demonstrate convergence of both gaps and clusters to front type solutions. Here, we see that the solutions begin at a perturbation of a constant state. Over the course of the continuation, the clusters and gaps converge to a state where the global maximums and global minimums coincide—these global maxima and minima correspond to the equilibria connected by the heteroclinic solution.

$\gamma = 1/16$:



$\gamma = 1/64$:



$\gamma = 1/256$:

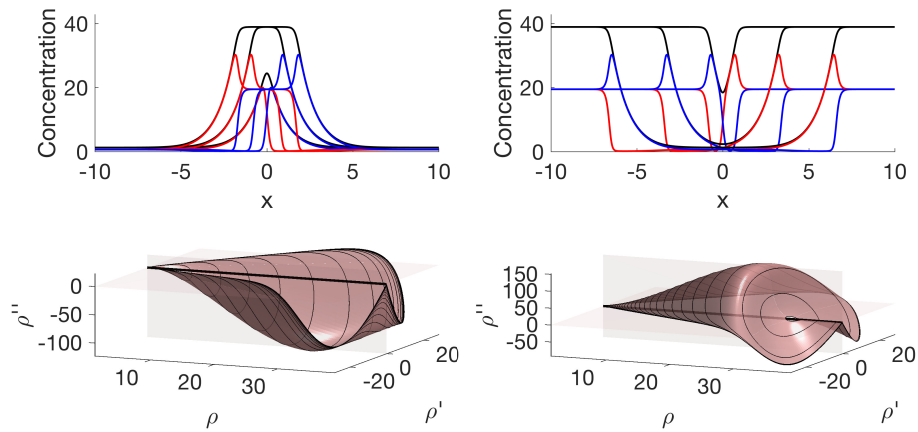


Figure 5: Spatial plots of cluster and gap solutions, with associated phase portraits for $\gamma = 1/16, 1/64, 1/256$ with $dx = 0.01, 0.025, 0.01$ respectively. In the 2D plots, we plot u in blue, v in red and ρ in black as functions of x . For the phase portraits, we plot the trajectories $(\rho(x), \rho'(x), \rho''(x))$ as black curves in 3D space. The collection of these families form a surface in phase space, shown in rust red.

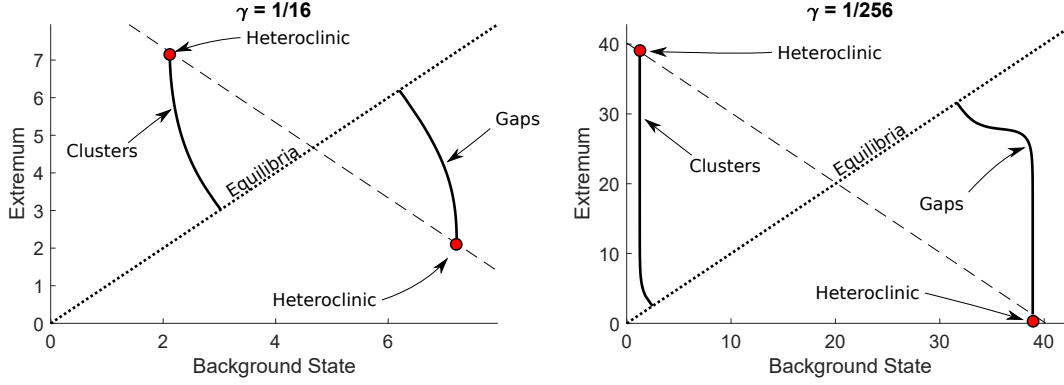


Figure 6: Maxima of clusters and minima of gaps in the continuation, plotted against the background state, for sample values of γ .

4.2 Heteroclinic continuation in the limit $\gamma \rightarrow 0$

Now, we present the results of numerical continuation of the heteroclinic solutions in the limit $\gamma \rightarrow 0$. From Section 2.2, we know such solutions exist for $0 < \gamma^* - \gamma \ll 1$. In figure 7, we provide a selection of profiles from this numerical continuation, accompanied by a plot illustrating the asymptotics of ρ under the limit $\gamma \rightarrow 0$. If we rescale ρ by $\tilde{\rho}(x) = \sqrt{\gamma}\rho(x)$, we observe a simple asymptotic structure that appears piecewise exponential—to illustrate this, we plot the logarithm of the rescaled profiles. Within a 10^{-5} margin of error, the maximum of $\rho\sqrt{\gamma}$ converges to $\sqrt{6}$. If we were to formally set $\gamma = 0$, the resulting ODE for $\tilde{\rho}$ admits solutions of the form $(\tilde{\rho})^2 = (\tilde{\rho}')^2$. Singular perturbation of this rescaled solution for small γ analysis may offer insight into the asymptotics of this continuation in greater detail.

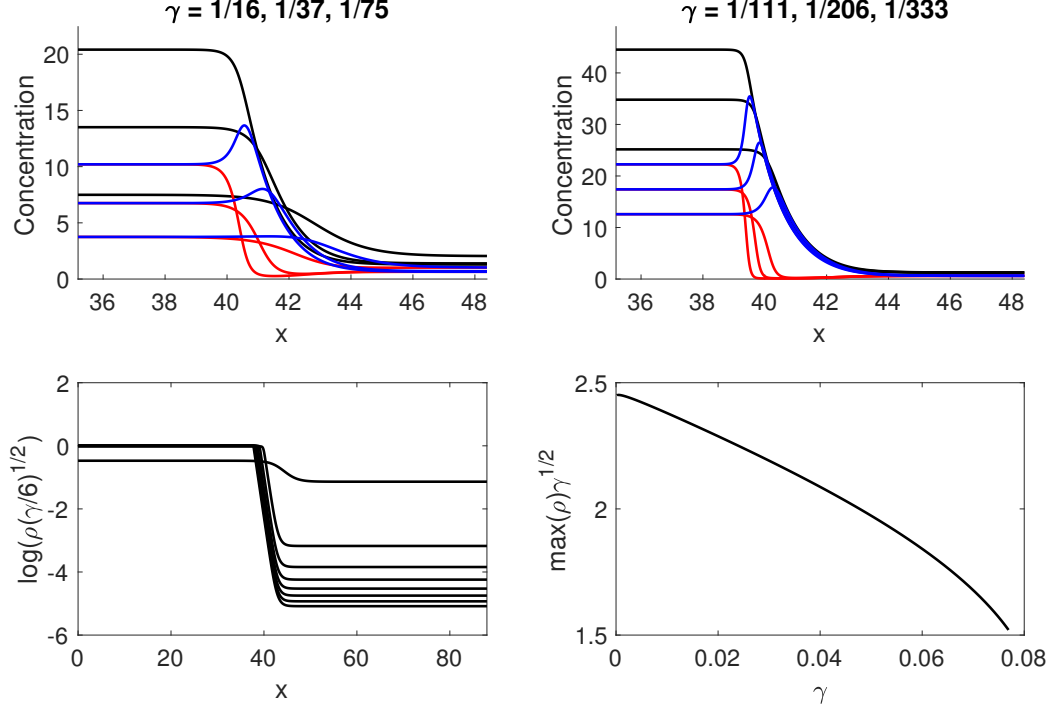


Figure 7: Heteroclinic profiles are plotted as γ varies from $\gamma = 1/13$ to $\gamma = 1/6639$. In the top two plots, we once again plot u in blue, v in red and ρ in black. The plot of $\log(\rho\sqrt{\gamma/6})^{1/2}$ exhibits the asymptotically simple structure of the heteroclinic. Bottom left shows the actual computational domain with grid size $dx = 0.088$.

4.3 Linear stability of homoclinic and heteroclinic solutions

Utilizing the continuation data of the previous two sections, we compute eigenvalue data using the method described in 3.4. In figure 8, we plot the 10 eigenvalues with largest real part using the profiles shown in figure 5 against the background concentration parameter ρ_∞ . Observe that the growth rates for $\gamma = 1/64$ and $\gamma = 1/256$ converge to nonpositive numbers, whereas positive growth rates persist in the heteroclinic limit for $\gamma = 1/16$.

In figure 9, we provide the same eigenvalue plot, but for the heteroclinic continuation on the left, with the fast convergence to a stable spectrum near $\gamma \approx 1/3.9^2$ magnified. We complement this plot with another plot, shown to the right, where we compare the two background concentrations of the front against the region where constant solutions are linearly unstable. From [3], we have the explicit formula for this region, given by the range

$$\left(\sqrt{\frac{1 - 2\gamma - \sqrt{1 - 8\gamma}}{2\gamma(1 + \gamma)}}, \sqrt{\frac{1 - 2\gamma + \sqrt{1 - 8\gamma}}{2\gamma(1 + \gamma)}} \right), \quad (30)$$

having set $\mu = 1$. We observe that the the point where the fronts become stable approximately coincides with the value of γ where the the front's extreme values exit the region of instability. We can reconcile this numerical observation with a loose theoretical argument: at large spatial scales, we can approximate front solutions as

$$\rho(x) \approx \begin{cases} \sup_{x \in \mathbb{R}} \rho(x) & \text{for } x < x_0, \\ \inf_{x \in \mathbb{R}} \rho(x) & \text{for } x > x_0, \end{cases} \quad (31)$$

where x_0 is an approximate location of the interface of the front solution. Therefore, we expect that the stability of a front should coincide with the stability of the solution's extreme values.

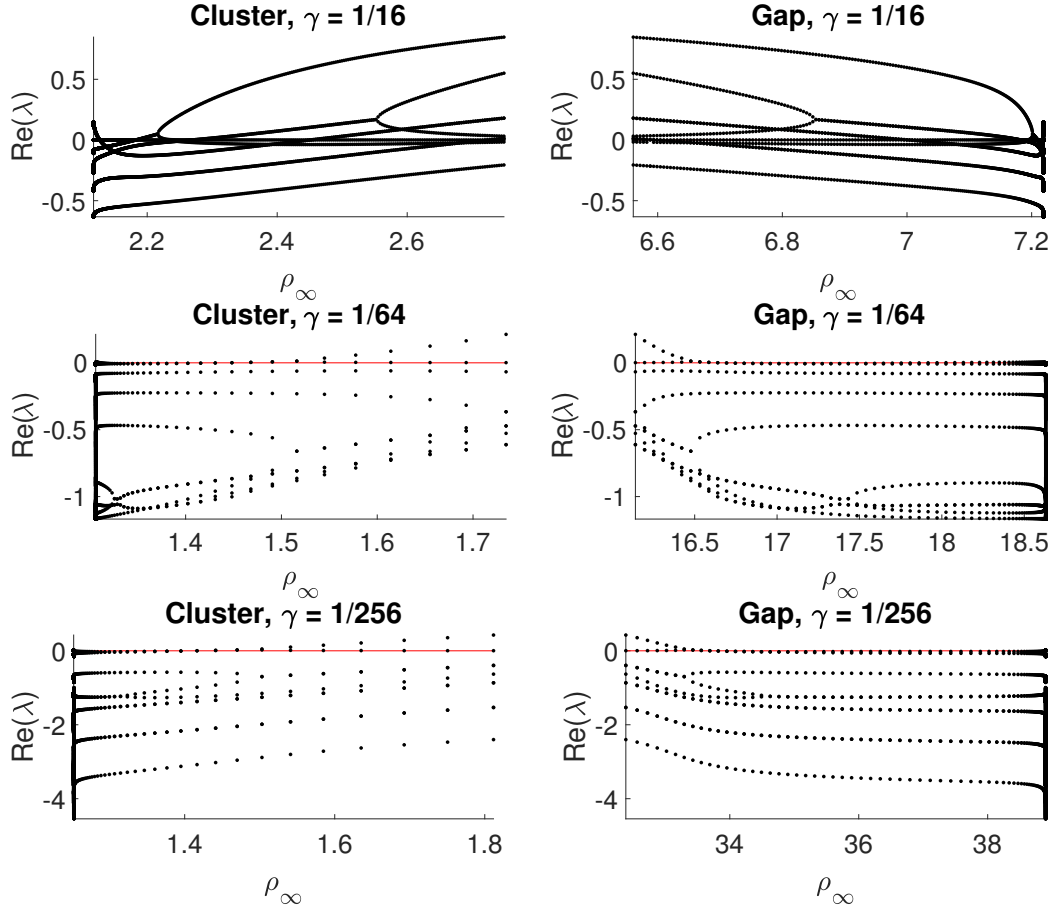


Figure 8: Spectra of clusters and gaps as functions of the background ρ_∞ , for various values of γ . Note that eigenvalues with positive real parts exist for gaps and clusters with large or small ρ_∞ , that is, near small-amplitude or heteroclinic limit, respectively.

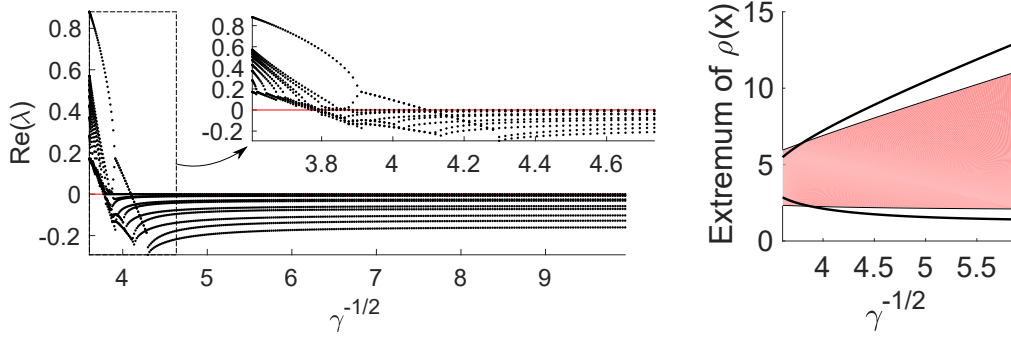


Figure 9: Left, we have the real part of the spectrum of the heteroclinics. Right, we have the two background concentrations of the heteroclinics in black (numerically the maximum and minimum of $\rho(x)$), and the region where the corresponding constant solutions are stable in pink. Computations here use grid size from the previous heteroclinic continuation.

4.4 Direct simulation of perturbed stationary profiles

For the concluding section of the numerical results section, we provide several samples of simulations of equation (2) using cluster, gap and front profiles with small perturbations in the direction of the most unstable eigenfunction. The first two samples, shown in figures 10 and 11, give examples of unstable cluster and gap profiles for $\gamma = 1/64$. The modes, both with growth rate ~ 1 , appear as antisymmetric and localized near the cluster or gap. These perturbations force the cluster or gap to transition to diffusive traveling waves. In the case of the cluster (figure 10), the bacterial population aligns its movement to the left, resulting in a diffusive traveling wave. The gap (figure 11) exhibits similar behavior, although this time movement aligns to the right, and the traveling wave broadens rather than shrinks. Contrary to intuition, the traveling wave moves to the right despite the left moving u dominating in the region where there is low concentration.

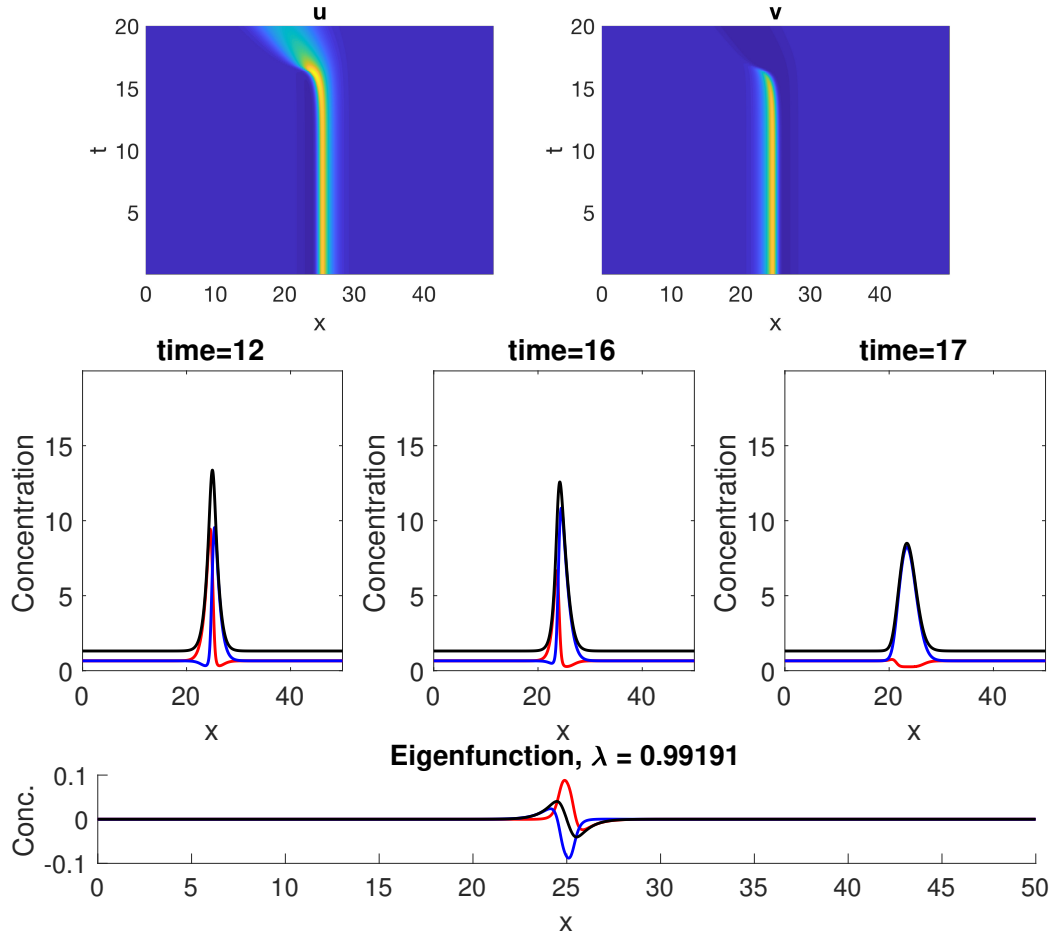


Figure 10: Concentrations u , v and ρ are plotted in space and time (top), three snapshots of the concentration profile with u , v and ρ plotted in blue, red and black respectively (middle) and the normalized eigenfunction perturbation used (bottom). Parameter values are $\gamma = 1/64$, and $\rho_\infty = 1.3115$.

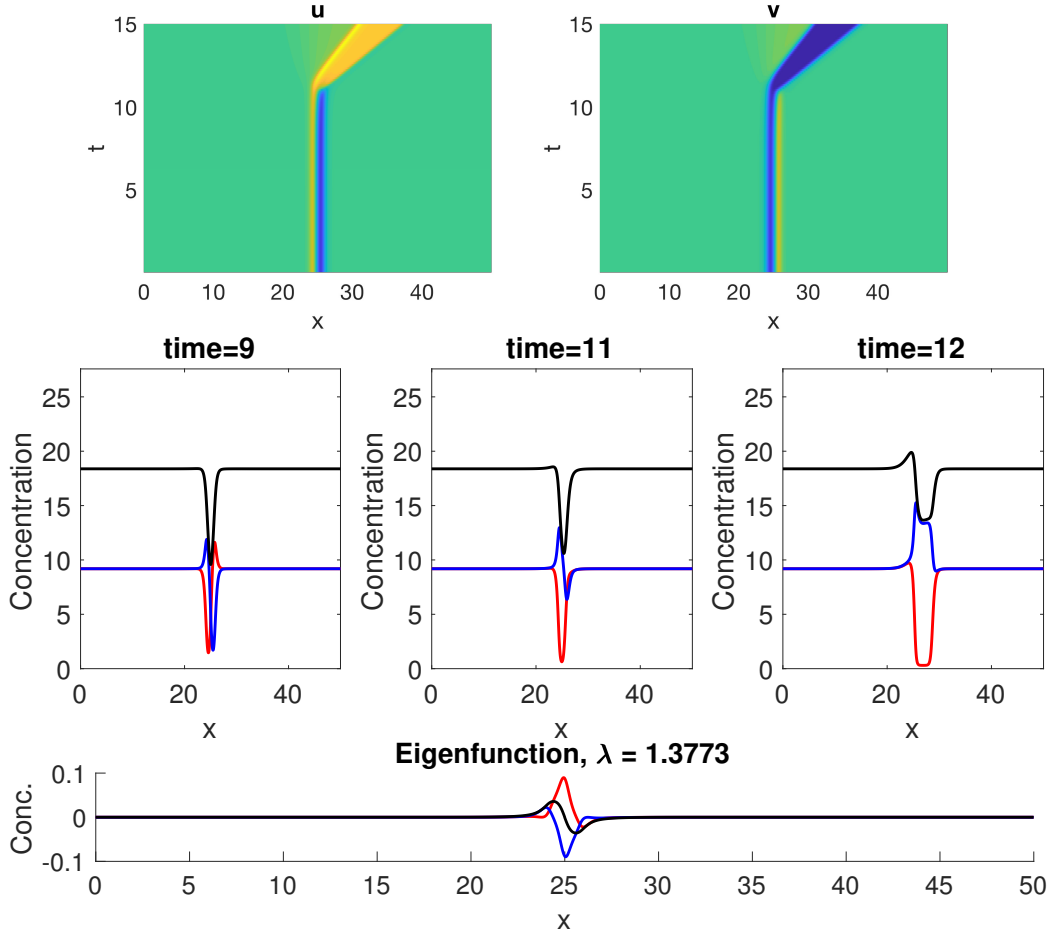


Figure 11: Concentrations u , v and ρ are plotted in space and time (top), three snapshots of the concentration profile with u , v and ρ plotted in blue, red and black respectively (middle) and normalized eigenfunction perturbation (bottom). Again, we plot u in blue, v red and ρ in black. Parameter values are $\gamma = 1/64$, and $\rho_\infty = 18.3805$.

Following these two figures, we provide a similar set of plots in figure 12 for an unstable heteroclinic solution at $\gamma = 1/13.81$. We reflect this solution about $x = 0$, to get a broad cluster solution. Now, the perturbation is localized to the two interfaces of the cluster. The perturbation to the right interface has significantly larger amplitude than the left perturbation, indicating that the eigenvalue problem is degenerate and the dynamics at the two interfaces are decoupled. This order of magnitude difference has little effect on the growth of the instability over the course of the simulation, where we see the two interfaces symmetrically transition into a state that favors either the left or right moving population.

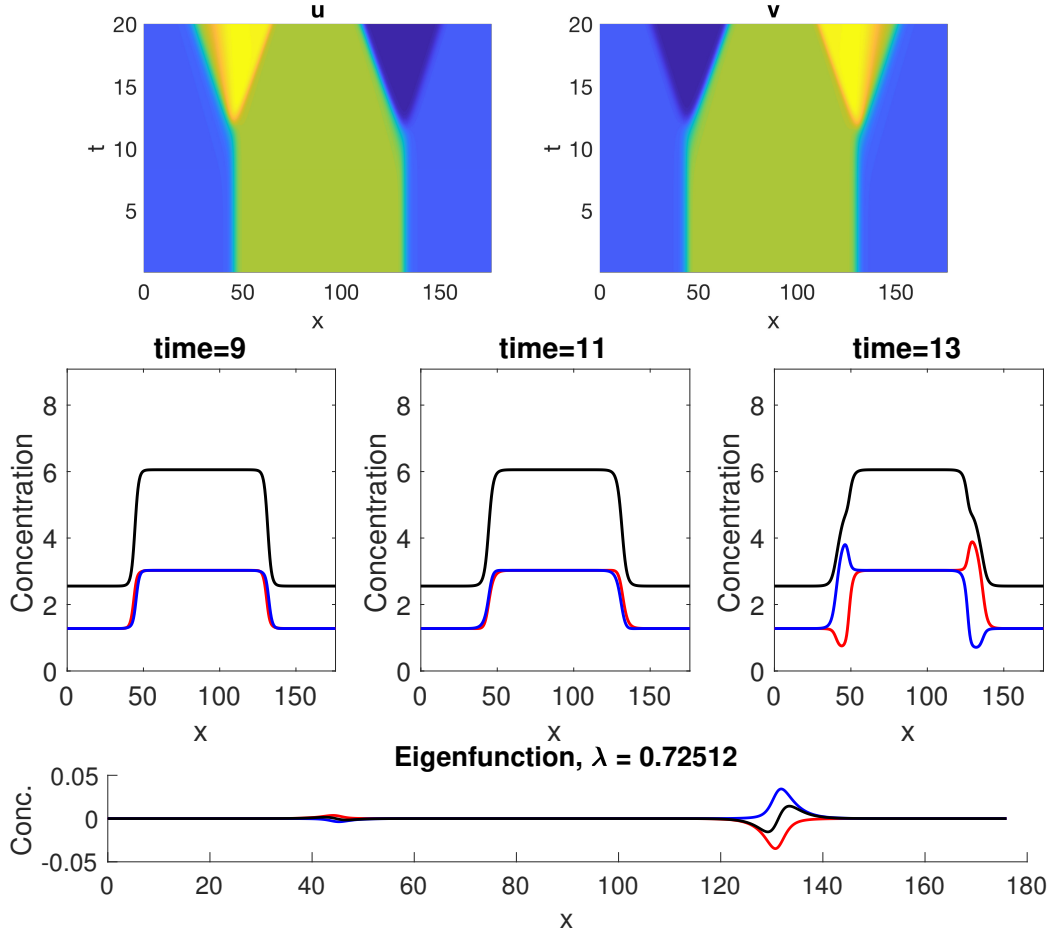


Figure 12: Concentrations u , v and ρ are plotted in space and time (top), three snapshots of the concentration profile with u , v and ρ plotted in blue, red and black respectively (middle), and normalized eigenfunction perturbation (bottom). Again, we plot u in blue, v red and ρ in black. Here, we use $\gamma = 1/13.81$.

In figure 13, we apply the same perturbation procedure to stable clusters. Again, we use the eigenfunction with largest real part to perturb the profile. Showing the time-evolution of the profile as we did for the unstable solutions is uninformative here. So, we instead plot the logarithm of L^2 (square integral norm) of (u_t, v_t) , demonstrating miniscule growth consistent with nearly zero eigenvalues. Observe that in contrast to the antisymmetry of the unstable eigenfunctions, the eigenfunctions here are symmetric. In figure 14, we give the same set of plots for the perturbation of a stable front solution.

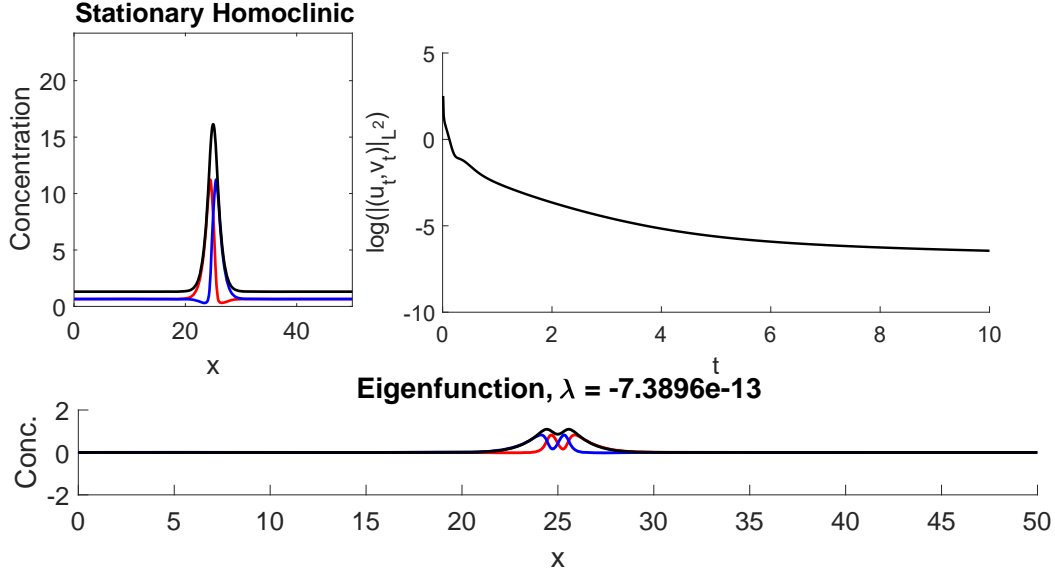


Figure 13: Top right is a plot of a cluster with a stable spectrum (top right), its eigenfunction with largest growth rate (bottom) and decay of the growth of perturbation by this eigenfunction as the logarithm of the L^2 norm of (u_t, v_t) (top left). Again, we plot u in blue, v red and ρ in black. Parameter values are $\gamma = 1/64$, $\rho_\infty = 1.3072$.

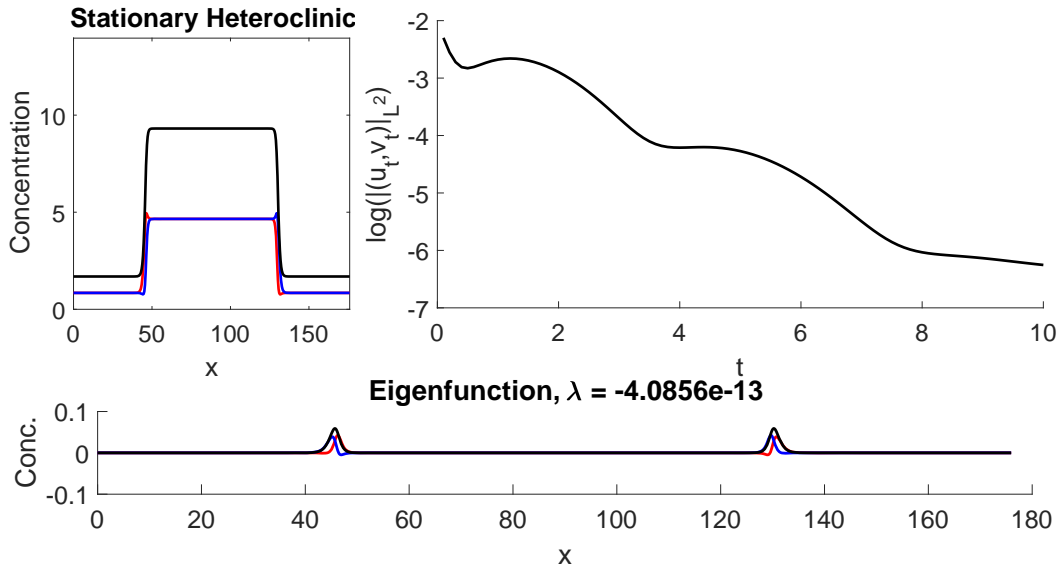


Figure 14: Top right is a plot of a reflected front solution with a stable spectrum (top right), the eigenfunction with largest growth rate (bottom) and decay in time of the growth of perturbation by this eigenfunction as the logarithm of the L^2 norm of (u_t, v_t) (top left). Again, we plot u in blue, v red and ρ in black. Here, $\gamma = 1/21.41$.

4.5 Discussion

Our numerical results corroborate our theoretical observations. Beginning with the continuations of clusters and gaps in Section 4.1, we verified that the families of clusters and gaps begin with perturbations of constant solutions, and limit on a front solution.

The remainder of our numerical results extend our analysis in two ways: first, we have evidence for the existence of front solutions for small $\gamma > 0$ as in Section 4.2; second, we have various simulations indicating the (in)stability of stationary solutions. The eigenvalue computations of 4.3 suggest that the clusters, gaps and fronts generally become stable for sufficiently small γ . Moreover, clusters and gaps appear to become more stable as they approach the front limit (cf. figure 8). The subsequent direct simulations of Section 3.5 provide some verification of the spectral computations, with positive growth rates coinciding with instability, and nonpositive growth rates coinciding with stability. The appearance of zero eigenvalues in the linear stability eigenvalue problem indicates the potential for nonlinear instabilities. However, this is not the case in the simulations we ran, with the growth of perturbations decaying over long time intervals. Generally, it appears that instabilities arise from antisymmetric modes that produce diffusive transport of concentration.

5 Conclusion

By only including diffusion and run-and-tumble dynamics to model the myxobacteria, we demonstrate a minimalist picture of what drives the formation of fruiting bodies in experiment. In section 2, we are able to establish the existence of stationary cluster, front and gap type solutions by analyzing the spatial ODE of stationary solutions and exploiting the symmetry inherent in the equation. We also see that these three types of solutions belong to a larger family, in the sense that the cluster and gap solutions both limit on a unique front solution. The numerical continuation experiments in section 4 further demonstrate this phenomena. We also saw that the clusters and gaps exist only below a critical value of γ . Seeing that nonlinearity of the tumbling rate increases in significance as $\gamma \rightarrow 0$, this serves as some verification that a nonlinear tumbling rate is necessary in order to produce clustering.

Although our numerical and theoretical results are in accordance with our hopes for this equation to model clustering, there are several questions that have not been addressed here. Two of these pertain to analysis: first, we made no attempt at a rigorous treatment of stability of these solutions. Second, although we have some knowledge about the existence of fronts for γ less than and close to $(8\mu + 4)^{-1}$, their existence in the limit $\gamma \rightarrow 0$ remains open.

From the perspective of modeling, this study may be unsatisfying in two ways. First, our results are specific to a very particular tumbling rate. We have little reason to believe that the tumbling rate takes on the form we prescribe here. Second, our

model is hampered by being restricted to one spatial dimension, whereas the spatial patterns of the myxobacteria clearly exist in (at least) two dimensions. The first of these issues is largely superficial, as the perturbation and geometric techniques we use here are general to a large class of turning rates. The second issue, on the other hand, is far more imposing—even establishing a meaningful model in two-dimensions is no easy task, since bacteria can move along any angle, rather than just left or right. Nevertheless, our study provides confirmation that run-and-tumble dynamics coupled with dampening via brownian motion are sufficient to produce structures resembling the fruiting bodies shown in the introduction (figure 1). Given that these two features, run-and-tumble and brownian motion, should manifest in more realistic models of *M. xanthus* populations, we hypothesize that these mechanisms drive clustering of actual cells.

Acknowledgements

Thank you Dr. Arnd Scheel for the extensive support over the last year. Thank you Dr. Bo Sun for offering frank and excellent feedback on this project. Thank you Dr. Radu Dascaliuc introducing me to the world of mathematics research. Thank you Dr. Janet Tate for the breadth of advice on scientific writing, and the encouragement to see this project through.

Most of the material presented here is the product of the “Complex Systems” REU at University of Minnesota, funded by the NSF grant DMS-1311740. A preprint of a submitted article showing much of the same material can be found in [17].

6 Appendix

Here, we provide two results that we use in Section 2.2. The first of these also provides the theoretical basis for the continuation methods described in Section 3.1. For a more general treatment of the same result, see [18].

Theorem (Implicit Function Theorem). *Let $F_c : \mathbb{R}^n \times \mathbb{R} \rightarrow \mathbb{R}^n$ be a family of functions that are continuously differentiable in the parameter c . Suppose there are $\mathbf{x}_0 \in \mathbb{R}^n$ and $c_0 \in \mathbb{R}$ such that $F_{c_0}(\mathbf{x}_0) = 0$ and the Jacobian of F_c is invertible at \mathbf{x}_0 . Then there is a smooth curve $\mathbf{x} : I \rightarrow \mathbb{R}^n$, where I is an interval neighborhood of c_0 , such that $\mathbf{x}(c_0) = \mathbf{x}_0$ and $F_c(\mathbf{x}(c)) = 0$ for all $c \in I$.*

Next, we have the Unstable Manifold Theorem, adapted from Theorem 4.1 of [19]. We consider the ODE $F(\mathbf{x}(t)) = \mathbf{x}'(t)$. We denote the Jacobian matrix of F at \mathbf{x} by $DF(\mathbf{x})$. Loosely speaking, the Stable Manifold Theorem states that near an equilibrium point (which after translation, we fix to be the origin), the solution behaves like a solution to the linear approximation of the ODE (given by $DF(0)(\mathbf{x}(t)) = \mathbf{x}'(t)$). This Theorem provides the existence of the unstable manifold, or a set that converges

asymptotically to the equilibrium solution in the limit $t \rightarrow -\infty$. In our application, these manifolds are just a smooth curves in \mathbb{R}^3 , as shown in figure 3.

Theorem (Unstable Manifold Theorem). *Suppose the function F is a continuously differentiable function from \mathbb{R}^n to \mathbb{R}^n and $F(0) = 0$. We then take \mathbf{x} to be a solution to the problem*

$$\begin{aligned} F(\mathbf{x}(t)) &= \mathbf{x}'(t) \text{ for all } t \in \mathbb{R}, \\ \mathbf{x}(0) &= \mathbf{x}_0, \end{aligned}$$

where I is a neighborhood of t . We assume that, up to a change of basis, the Jacobian matrix of F at 0 may be written in block diagonal form:

$$DF(0) = \begin{pmatrix} S & 0 \\ 0 & T \end{pmatrix}$$

where S is a $k \times k$ matrix and T is a $l \times l$ matrix (here, $k+l = n$). We suppose further that there are constants $a < b$ for which all eigenvalues of S have real part strictly less than a , and eigenvalues of T have real part strictly larger than b . Finally, assume that $\int_{\mathbb{R}^n} \|F(\mathbf{x}) - DF(\mathbf{x}_0)\mathbf{x}\| d\mathbf{x}$ is sufficiently small. Under these assumptions, there exists a unique function $\alpha : \mathbb{R}^k \rightarrow \mathbb{R}^l$ with bounded and continuous derivative $D\alpha$ with the following properties:

1. We have $\alpha(0) = 0$, $D\alpha(0) = 0$. In other words, the tangent plane of α at 0 is given by the direct sum of eigenspaces of $DF(0)$ whose eigenvalues have real part less than a .
2. Suppose \mathbf{x}_0 is in the graph of α , i.e. $\mathbf{x}_0 = (\mathbf{u}_0, \alpha(\mathbf{u}_0))$ for some $\mathbf{u}_0 \in \mathbb{R}^k$. Then $\mathbf{x}(t)$ is also in the graph of α for all t . Moreover, for all $\lambda > a$, there exists a constant C such that

$$\|\mathbf{x}(t)\| \leq C\|\mathbf{u}_0\| \exp(\lambda t).$$

By replacing t with $-t$, we get the Stable Manifold Theorem, which provides the same result but for solutions converging to 0 forward in time.

References

- [1] J. Berleman, “Myxococcus xanthus preying on an e. coli colony.” <https://www.youtube.com/watch?v=tstc6doiNCU>, 2013. Accessed 9/1/2017.
- [2] F. Lutscher, A. Stevens, *et al.*, “Emerging patterns in a hyperbolic model for locally interacting cell systems,” *Journal of Nonlinear Science*, vol. 12, no. 6, pp. 619–640, 2002.
- [3] A. Scheel and A. Stevens, “Wavenumber selection in coupled transport equations,” *Journal of Mathematical Biology*, pp. 1–27, 2016.

- [4] E. Palsson and H. G. Othmer, “A model for individual and collective cell movement in dictyostelium discoideum,” *Proceedings of the National Academy of Sciences*, vol. 97, no. 19, pp. 10448–10453, 2000.
- [5] A. Tero, R. Kobayashi, and T. Nakagaki, “A mathematical model for adaptive transport network in path finding by true slime mold,” *Journal of theoretical biology*, vol. 244, no. 4, pp. 553–564, 2007.
- [6] C. Xue, E. O. Budrene, and H. G. Othmer, “Radial and spiral stream formation in proteus mirabilis colonies,” *PLoS computational biology*, vol. 7, no. 12, p. e1002332, 2011.
- [7] J. E. Berleman, T. Chumley, P. Cheung, and J. R. Kirby, “Rippling is a predatory behavior in myxococcus xanthus,” *Journal of bacteriology*, vol. 188, no. 16, pp. 5888–5895, 2006.
- [8] B. Sager and D. Kaiser, “Intercellular c-signaling and the traveling waves of myxococcus,” *Genes & Development*, vol. 8, no. 23, pp. 2793–2804, 1994.
- [9] M. Kac, “A stochastic model related to the telegrapher’s equation,” *The Rocky Mountain Journal of Mathematics*, vol. 4, no. 3, pp. 497–509, 1974.
- [10] S. Goldstein, “On diffusion by discontinuous movements, and on the telegraph equation,” *The Quarterly Journal of Mechanics and Applied Mathematics*, vol. 4, no. 2, pp. 129–156, 1951.
- [11] P. Degond and A. Manhart, “Hui yu. a continuum model for nematic alignment of self-propelled particles,” *Discrete & Continuous Dynamical Systems-B*, vol. 22, no. 4, pp. 1295–1327, 2017.
- [12] A. M. Turing, “The chemical basis of morphogenesis,” *Philosophical Transactions of the Royal Society of London B: Biological Sciences*, vol. 237, no. 641, pp. 37–72, 1952.
- [13] J. K. Hale, “Asymptotic behavior of dissipative systems,” 1987.
- [14] H. B. Keller, “Numerical solution of bifurcation and nonlinear eigenvalue problems,” *Applications of bifurcation theory*, 1977.
- [15] E. J. Doedel, “Lecture notes on numerical analysis of nonlinear equations,” in *Numerical Continuation Methods for dynamical systems*, pp. 1–49, Springer, 2007.
- [16] E. L. Allgower and K. Georg, *Numerical continuation methods: an introduction*, vol. 13. Springer Science & Business Media, 2012.
- [17] P. Flynn, Q. Neville, and A. Scheel, “Self-organized clusters in diffusive run-and-tumble processes,” *arXiv preprint arXiv:1712.00112*, 2017.

- [18] M. Spivak, *Calculus On Manifolds: A Modern Approach To Classical Theorems Of Advanced Calculus*. Mathematics monograph series, Avalon Publishing, 1971.
- [19] C. Chicone, *Ordinary Differential Equations with Applications*. Texts in applied mathematics, Springer, 1999.